LA-UR-21-21045
Approved for public release; distribution is unlimited.

Title: A viscoelastic viscoplastic damage model (VPVD)

Author(s): Buechler, Miles Allen
Luscher, Darby Jon
Miller, Nathan Andrew

Intended for: Report

Issued: 2021-02-05 (rev.1)

A viscoelastic viscoplastic damage model (VPVD)

Miles A. Buechler, D.J. Luscher, Nathan Miller

Los Alamos National Laboratory

Los Alamos, NM 87545

buechler@lanl.gov

Chapter 1

Introduction

This report documents the development, implementation, and parameter estimation procedures for a viscoelastic-viscoplastic-viscodamage model. This model is being developed to improve the predictive accuracy of simulations involving plastic bonded explosives (PBX). A representative PBX is PBX9501, which is 95% by weight HMX, 2.5% estane binder and 2.5% nitroplasticizer. Mechanical deformation of this material is primarily accommodated by straining of the polymer binder and rearranging the relatively rigid HMX crystals.

PBX9501 has been shown to exhibit viscoelastic, inelastic, and damage responses in experiments [6]. In this report viscoelastic response is defined as a rate dependent deformation response to external loads. Viscoelastic strain will return to zero given adequate unloaded recovery time. Inelastic response is defined as a response to external stimuli that will not return to zero over any unloaded recovery period. Damage is defined as a degradation of the material stiffness [11]. The degradation of the stiffness may be due to decohesion of binder and crystals, void growth in the binder, polymer chain damage in the binder, or other unknown mechanisms, but the model developed here simply treats it as a scalar loss of stiffness.

The viscoelastic nature of the material has been previously documented and models were developed to incorporate it [5]. Because the binder dominates the response, early constitutive models focused on the phenomenological linear viscoelastic models developed for accurate predictions of polymeric materials. These constitutive models lacked the fidelity to accurately predict the departure from linear viscoelastic behavior [16].

The damage response is also a well known part of the material behavior. ViscoSCRAM is a phenomenological model that combines linear viscoelasticity and brittle damage response to better predict the behavior of PBXs [4], [5], [13], [8] . The ViscoSCRAM material model only incorporates viscoelasticity and damage into the shear response. This results in non-physical behavior for high-triaxiality stress states. ViscoSCRAM also lacked an inelastic deformation mechanism, which results in poor predictive accuracy for cyclic loading.

The model development is documented in Chapter 2. In Chapter 3, a series of cyclic experiments is discussed as well as techniques for estimating model parameters from these experiments. A very limited validation study was performed and is documented in Chapter 4. Finally, Chapter 5 contains concluding remarks and future plans.

Direct notation is used throughout this report. In equations bold font is used for 2^{nd} order tensors, and blackboard font is used for 4^{th} order tensors. One example is the 2^{nd} order identity tensor ($\boldsymbol{i}$), the elements of which are δ_{ij}. Another example is the symmetric 4^{th} order identity tensor ($\mathbb{I}$), the elements of which are $\frac{1}{2}\left(\delta_{ik}\delta_{jl} + \delta_{il}\delta_{jk}\right)$. The tensor product is used in the definition of the tangent stiffness tensor. It is written $\boldsymbol{A} \otimes \boldsymbol{B}$ and the elements are $A_{ij}B_{kl}$.

Chapter 2

Model Development

The model documented within this report incorporates viscoelastic response and a viscous model for both plastic and damage evolution phenomena. These phenomena are supported by experimental data that is discussed in Chapter 3. The model is based on small strain kinematics as described in Section 2.1. The viscoelastic response is determined using a generalized Maxwell model [9]. There are other potential viscoelastic models such as Kelvin-Voight [9], but W-13 has over a decade of experience developing and fitting Maxwell models to experimental data. Section 2.2 contains pseudo-code for evaluating the Maxwell model. The damage model is defined in Section 2.3. The overstress model that provides the kinetics of plastic deformation is described in Section 2.4. Temperature dependance is briefly discussed in Section 2.5. A solution algorithm is presented in Section 2.6, and the elastic tangent stiffness tensor, which is required for global iteration in an implicit code, is discussed in Section 2.7.

2.1 Kinematics

This constitutive model is based on small strain theory. The total strain can be partitioned into deviatoric and volumetric parts by

$$\boldsymbol{\epsilon} = \boldsymbol{e} + \frac{1}{3} E \boldsymbol{i}, \tag{2.1}$$

where $\boldsymbol{\epsilon}$ is the total strain tensor, $\boldsymbol{e}$ is the deviatoric strain tensor, E is the volumetric strain, and $\boldsymbol{i}$ is the second order identity tensor. Small strain theory allows us to further decompose the deviatoric and volumetric strains into inelastic ($\boldsymbol{e}^i$, and E^i) and recoverable ($\boldsymbol{e}^r$, and E^r) parts following

$$\boldsymbol{e} = \boldsymbol{e}^i + \boldsymbol{e}^r, \tag{2.2}$$

$$E = E^i + E^r. \tag{2.3}$$

The recoverable strain is further decomposed to account for damage such that

$$\boldsymbol{e}^{ve} = (1 - D)\, \boldsymbol{e}^r \tag{2.4}$$

$$E^{ve} = (1 - D)\, E^r, \tag{2.5}$$

where $\boldsymbol{e}^{ve}$ and E^{ve} are the deviatoric and volumetric strain measures that relate directly to stress. D is a scalar damage variable that relates the damaged stiffness to the undamaged stiffness. The stress response to the viscoelastic strain is determined using a Maxwell model. The viscoelastic evolution equations are discussed in Section 2.2. Perzyna-like viscosity equations are used to evaluate the damage and inelastic strain evolution as discussed in Sections 2.3, and 2.4 respectively.

2.2 Stress strain relations

The stress tensor is also partitioned into deviatoric and volumetric components as

$$\boldsymbol{\sigma} = \boldsymbol{S} + \sigma_m \boldsymbol{i} \tag{2.6}$$

where $\boldsymbol{\sigma}$ is the total stress tensor, $\boldsymbol{S}$ is the deviatoric stress tensor, and σ_m is the mean stress. The deviatoric stress can be related to the viscoelastic portion of the deviatoric strain through the convolution integral

$$\boldsymbol{S}(t) = \int_{\zeta=0}^{\zeta=t} 2G(t-\zeta)\,\dot{\boldsymbol{e}}^{ve}(\zeta)\,d\zeta \tag{2.7}$$

where, in this implementation, the shear stiffness, $G(t)$ is modeled with a Prony Series defined as

$$G(t) = G^{\infty} + \sum_{j=1}^{N} G^{(j)} \exp\left[\frac{-t}{\tau^{(j)}}\right]. \tag{2.8}$$

G^{∞}, the $G^{(j)}$, and the $\tau^{(j)}$ are fitting parameters, whose physical meaning is described in the literature and summarized in [8]. The variable t is time in the same units as $\tau^{(j)}$.

The mean stress could be treated in a similar way; however, the limited experimental data that exists supports using a constant bulk modulus rather than a viscoelastic volumetric response thus, the linear elastic equation for the mean stress is

$$\sigma_m = KE^{ve}, \tag{2.9}$$

where K is the elastic bulk modulus.

Solution schemes for the viscoelastic stress-strain relation are widely documented in the literature, for example see [2], [9], or [13]. The particular scheme employed in this model is summarized in Algorithm 1. The term $\boldsymbol{\xi}^{(j)}$ in the algorithm is a deviatoric internal variable that is analogous to strain. The evolution of $\boldsymbol{\xi}^{(j)}$ is related to viscous relaxation. The algorithm requires the parameters G_0, $G^{(j)}$, and $\tau^{(j)}$, but G_0 can be found by evaluating Equation 2.8 at $t = 0$, which results in $G_0 = G^{\infty} + \sum_{j=1}^{N} G^{(j)}$.

Algorithm 1 Maxwell [2]

Input: VARS : $\Delta\mathbf{e}^{ve}$, Δt, $\mathbf{e}_n^{ve}$, $\boldsymbol{\xi}_n^{(j)}$ PARAMS : $G_0, G^{(j)}, \tau^{(j)}$

1: $\Delta\boldsymbol{\xi}^{(j)} = \left(1 - \exp\left[\frac{-\Delta t}{\tau^{(j)}}\right]\right)\left(\mathbf{e}_n^{ve} - \boldsymbol{\xi}_n^{(j)}\right) + \frac{\tau^{(j)}}{\Delta t}\left(\frac{\Delta t}{\tau^{(j)}} + \exp\left[\frac{-\Delta t}{\tau^{(j)}}\right] - 1\right)\Delta\mathbf{e}^{ve}$

2: $\boldsymbol{\xi}_{n+1}^{(j)} = \boldsymbol{\xi}_n^{(j)} + \Delta\boldsymbol{\xi}^{(j)}$

3: $\mathbf{S}_{n+1} = G_0\left(\mathbf{e}_{n+1} - \sum_{j=1}^{N}\frac{G^{(j)}}{G_0}\boldsymbol{\xi}_{n+1}^{(j)}\right)$

4: $G^T = G_0 - \sum_{j=1}^{N}\frac{G^{(j)}\tau^{(j)}}{\Delta t}\left[\frac{\Delta t}{\tau^{(j)}} - \left(1 - \exp\left[\frac{-\Delta t}{\tau^{(j)}}\right]\right)\right]$

Output: $\mathbf{S}_{n+1}$, $\boldsymbol{\xi}_{n+1}^{(j)}$, G^T

2.3 Damage Evolution

Several observations guided the development of the damage kinetics model documented in this section. First, the magnitude of damage evolution is dependent on strain rate and temperature. Second, experimental results indicate that there is no threshold surface in stress space inside of which damage evolution is completely suppressed [7]. This observation applies to the uniaxial tension and uniaxial compression experiments discussed in Chapter 3, but it is reasonable to believe that damage growth could be suppressed for stress states with a sufficiently negative triaxiality, $\frac{\sigma_m}{\bar{\sigma}}$ [2]. Third, while no discernible critical surface was observed, we did observe a reduced damage rate for a given stress in subsequent cycles leading us to believe that there is a hardening phenomena associated with damage evolution.

The damage kinetics model we have implemented is similar to a Perzyna model commonly utilized for viscoplastic evolution [10]. Perzyna models are often referred to as overstress models, because unlike rate independent evolution equations or models with rate dependent threshold surfaces such as Johnson Cook [12], a state of stress that exist outside of the threshold surface is admissible. The evolution rate is then proportional to how far the the state of stress is outside the threshold surface, and the threshold

surface can expand or contract with damage evolution. The Perzyna model is described mathematically as

$$\dot{D} = \left\langle \frac{f^d(\boldsymbol{\sigma}, q)}{\tau^d} \right\rangle^{n^d}, \tag{2.10}$$

where $\dot{D}$ is the damage rate, f^d is a function defining the proximity of the stress state to the threshold surface. The size of the threshold surface is defined in terms of the scalar q which is a function of the current damage D. The viscosity, τ^d, defines the relaxation rate, and the shape factor, n^d provides the shape of the transition from rate independent to rate dependent behavior [10]. Both f^d and τ^d have units of stress. $< \bullet >$ are Macaulay brackets that return the argument for values greater than zero, or return zero when the argument is less than zero, effectively providing a threshold surface.

In the new model, the function f^d is a Drucker-Prager equivalent stress defined as $\sigma^* = \bar{\sigma} + B^d \sigma_m$ [15], where $\bar{\sigma}$ is the Von-Mises stress, and B^d is the damage rate pressure proportionality constant. The Drucker-Prager effective stress introduces the observed pressure dependence. The Perzyna overstress viscosity, τ^d, is assumed to be a function of damage and is subject to the restriction that $\tau^d > 0$ for all $0 \leq D \leq 1$ so that the intended threshold surface is retained. Stress states associated with uniaxial tension cannot exist inside the critical surface and, as long as $B^d < 3$, stress states under uniaxial compression will never exist inside the critical surface. In other words, consistent with the earlier observations, uniaxial experiments will not exhibit a region of stresses where damage growth is entirely suppressed. We include the effects of damage on the stress state by introducing a damaged effective stress

$$\hat{\sigma} = \frac{\bar{\sigma} + B^d \sigma_m}{1 - D}, \tag{2.11}$$

such that the effective stress and therefore damage growth rate increases with increasing magnitudes of damage.

Equations 2.4 and 2.5 reflect the effect of damage in terms of the change to the recoverable response,

but to motivate Equation 2.11 refer to Figure 2.1. In the 1-D example the average stress far from the damage is $\sigma = F/A$. Near the damage, the area capable of carrying load is reduced to $(1-D)A$, resulting in an enhanced average stress of $\sigma/(1-D)$. In our development we are asserting that damage grows as a function of the enhanced average stress in the region of the damage.

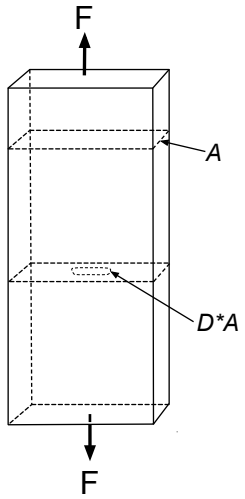

Figure 2.1: 1-D effective area example

Finally, temperature dependence is introduced using a function of temperature that premultiplies the quasi-Perzyna model resulting in

$$\dot{D} = \dot{D}_0 \left(T\right) \left\langle \frac{\hat{\sigma}}{\tau^d \left(D\right)} \right\rangle^{n^d}, \tag{2.12}$$

where $\dot{D}_0$ must be positive for all T, and as stated above τ^d is also positive for $0 \leq D \leq 1$. The scalar function $\dot{D}_0$ is discussed in Section 2.5

To further describe the evolution equations, the damage growth rate is depicted in Figure 2.2. The Macaulay bracket and constraints on τ^d result in the shaded region for which the damage growth rate is zero. This region is the result of a pressure (negative mean stress) that is large enough in proportion to the Von-Mises stress to suppress damage growth. The blue lines in the figure represent lines of constant damage growth rate. For a given temperature and current damage state any stress on the line will result in

the same instantaneous damage growth rate. The damage growth rate for the constant rate curve increases with increasing $\bar{\sigma}$ intercept. The red lines are uniaxial compression and uniaxial tension loading curves. The damage growth rate for a given Von-Mises stress is larger under uniaxial tension than under uniaxial compression.

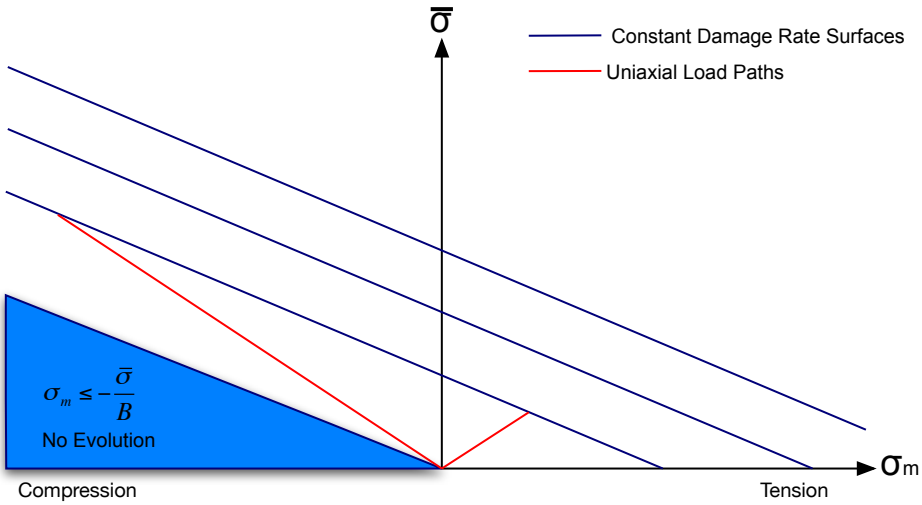

Figure 2.2: Damage rate surfaces in the Renduli Plane

To simplify model implementation a subroutine was written to evaluate Equation 2.12. This subroutine with the specific forms of τ^d is described in Algorithm 2. The form of the equation for τ^d was chosen to smoothly transition from a minimum value to a maximum value over the physically meaningful range of damage ($0 \leq D \leq 1$). However, for numerical stability we smoothly transition to a very high τ^d starting when D reaches a predetermined parameter D_L. D_L is typically around 0.99 which was found through numerical experimentation.

Algorithm 2 evolve_damage

Input: VARS : $\hat{\sigma}_k^d$, D_k PARAMS : m^d, τ_0^d, τ_L^d, D_L

$f^d = \hat{\sigma}_k^d$, $\frac{\partial f^d}{\partial \hat{\sigma}^d} = 1$

if $D \leq D_l$ **then**

  $\tau^d = \tau_0^d + \left(\tau_L^d - \tau_0^d\right) \sin\left(\frac{\pi}{2}\left(\frac{D}{D_L}\right)^{m^d}\right)$

  $\frac{\partial \tau^d}{\partial \Delta D} = \frac{m^d \pi}{2 D_L}\left(\tau_L^d - \tau_0^d\right)\left(\frac{D_k}{D_L}\right)^{m^d - 1} \cos\left(\frac{\pi}{2}\left(\frac{D_k}{D_L}\right)^{m^d}\right)$

else

  $\tau^d = \tau_L^d \tan\left(\frac{\pi(D_k - D_L)}{2 - 2D_L}\right)$

  $\frac{\partial \tau^d}{\partial \Delta D} = \frac{\pi}{2 - 2D_L}\left[1 + \tan\left(\frac{\pi(D_k - D_L)}{2 - 2D_L}\right)^2\right]$

end if

Output: f^d, τ^d, $\frac{\partial f^d}{\partial \hat{\sigma}^d}$, $\frac{\partial \tau^d}{\partial \Delta D}$

2.4 Plastic Evolution

The evolution of the inelastic strain tensor $\boldsymbol{\epsilon}^i$ is defined by a scalar rate equation $\dot{\lambda}$ and a flow tensor $\boldsymbol{\eta}$,

$$\dot{\boldsymbol{\epsilon}}^i = \dot{\lambda}\boldsymbol{\eta}. \tag{2.13}$$

The scalar rate equation, defined below, is similar to the damage rate equation 2.12.

$$\dot{\lambda} = \dot{\lambda}_0(T)\left\langle \frac{\hat{\sigma}^i}{\tau^i(\lambda)} \right\rangle^{n^i}, \tag{2.14}$$

where $\hat{\sigma}^i = \frac{\bar{\sigma} + B^i \sigma_m}{1 - D}$, and $\tau^i > 0$ for all λ. The flow tensor, $\boldsymbol{\eta}$, is a unit direction tensor. The direction is depicted on the Renduli plane by the green arrow in Figure 2.3. The model is developed such that β, the angle between the constant flow rate surface and the flow direction, is variable. However, at this time experimental data necessary for evaluating the angle is unavailable, so we assume associative flow.

Associative flow means that the flow is perpendicular to the flow surface or $\beta = 90°$. This results in maximal dissipation and assured stability [10], but for geo-materials has been shown to over predict the volumetric part of the inelastic strain.

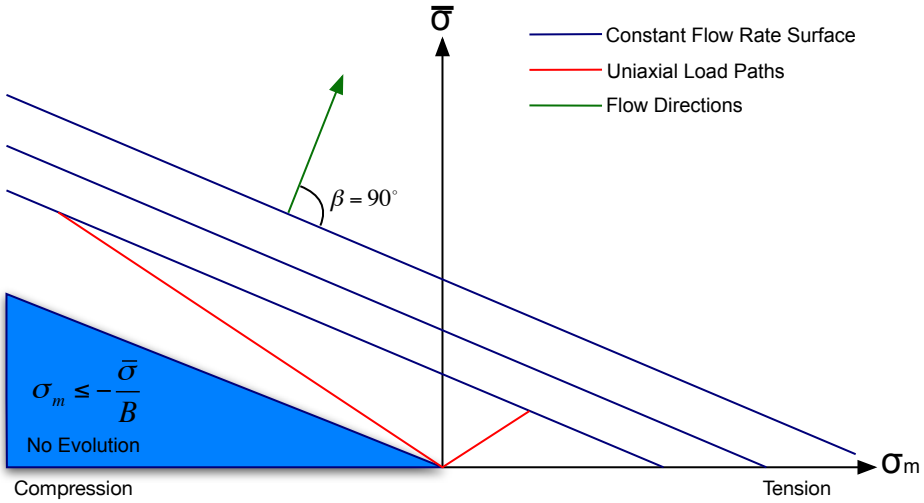

Figure 2.3: Flow rate surfaces in the Renduli Plane

The mathematical expression for the flow tensor is

$$\boldsymbol{\eta} = \frac{3}{\sqrt{\frac{3}{2} + \frac{B^2}{3}}}\boldsymbol{S} + \frac{B}{3\sqrt{\frac{3}{2} + \frac{B^2}{3}}}\boldsymbol{i}, \tag{2.15}$$

where B is related to B^i, and β. For instance, if $\beta = 90°$, then $B = B^i$. Again, to simplify model implementation a subroutine was written to evaluate Equation 2.13. This subroutine is represented in Algorithm 3. The value of τ^i remains constant when $\lambda \geq \lambda_L$, and in the idealized equations the derivative is zero. However, we have found that assigning a small positive number, e.g. 1E-8, to the derivative in this region is necessary to ensure convergence.

Algorithm 3 evolve_plastic

Input: VARS : $\hat{\sigma}_k^i,\ \lambda_k$ PARAMS : $m^i,\ \tau_0^i,\ \tau_L^i,\ \lambda_L$

Output: $f^i,\ \tau^i,\ \frac{\partial f^i}{\partial \hat{\sigma}^i},\ \frac{\partial \tau^i}{\partial \Delta\lambda}$

$f^i = \hat{\sigma}_k^i,\ \frac{\partial f^i}{\partial \hat{\sigma}^d} = 1$

if $\lambda \leq \lambda_l$ **then**

$\tau^i = \tau_0^i + \left(\tau_L^i - \tau_0^i\right) \sin\left(\frac{\pi}{2}\left(\frac{\lambda}{\lambda_L}\right)^{m^i}\right)$

$\frac{\partial \tau^i}{\partial \Delta\lambda} = \frac{m^i \pi}{2\lambda_L}\left(\tau_L^i - \tau_0^i\right)\left(\frac{\lambda_k}{\lambda_L}\right)^{m^i - 1} \cos\left(\frac{\pi}{2}\left(\frac{\lambda_k}{\lambda_L}\right)^{m^i}\right)$

else

$\tau^i = \tau_L^i$

$\frac{\partial \tau^i}{\partial \Delta\lambda} \approx 0$

end if

2.5 Temperature Dependence

Temperature dependence of the material is captured in this model using time-temperature-superposition [9]. Specifically, in the viscoelastic, the damage evolution, and the plastic flow models we use a shifted time step, Δt^*, which is calculated using the following functions:

$$\log(A) = \frac{-c_0\left(T - T_r\right)}{c_1 + T - T_r} \tag{2.16}$$

$$\Delta t^* = \frac{\Delta t}{A}, \tag{2.17}$$

where A is the shift, c_0 and c_1 are fitting parameters, T is the current temperature, and T_r is the reference temperature. c_0 and A are unit-less while c_1 has units of temperature. We note that there are potentially three sets of parameters, one set for each phenomenon.

2.6 Solution Algorithm

The integration of stress over a time increment is accomplished with a backward Euler implicit algorithm [3]. The change in total strain over the increment , $\Delta\boldsymbol{\epsilon}$, as well as the state variables at the beginning of the increment are passed from the parent code. The iteration begins with guessing the change in damage, ΔD, and equivalent inelastic strain $\Delta\lambda$. Then the change in recoverable strain is calculated, followed by the change in viscoelastic strain $\Delta\boldsymbol{\epsilon}^{ve}$. Next, the Maxwell model is applied to calculate the trial stress given the state variables and the change in viscoelastic strain. Finally, the rate of damage and inelastic strain are calculated using the trial stress and the error in the guesses is calculated using

$$\boldsymbol{E}_{rror} = \begin{bmatrix} \Delta\lambda \\ \Delta D \end{bmatrix} - \begin{bmatrix} \dot{\lambda}_0 \Delta t \Psi^i \left(\boldsymbol{\sigma}, D, \lambda\right) \\ \dot{D}_0 \Delta t \Psi^d \left(\boldsymbol{\sigma}, D\right) \end{bmatrix}, \tag{2.18}$$

where, for convenience, we have defined

$$\Psi^i = \left\langle \frac{f^i\left(\hat{\sigma}^i\right)}{\tau^i\left(\lambda\right)} \right\rangle^{n^i}, and \tag{2.19}$$

$$\Psi^d = \left\langle \frac{f^d\left(\hat{\sigma}^d\right)}{\tau^d\left(D\right)} \right\rangle^{n^d}. \tag{2.20}$$

This iteration process is summarized in Algorithm 4.

Algorithm 4 Incremental Damage and Plastic Strain Multiplier

Input: `VARS` : $\boldsymbol{\epsilon}_n$, $\Delta\boldsymbol{\epsilon}$, Δt, $\boldsymbol{\epsilon}^i_n$, $\boldsymbol{\xi}^{(j)}_n$, D_n

Input: `PARAMS` : $G_0, G^{(j)}, \tau^{(j)}$, K, B^i, B^r, B, m^i, m^d, n^i, n^d, τ^i_0, τ^i_L, g^d_0, g^d_L, D_L, λ_L

initialize: $k \leftarrow 0$, $\Delta\lambda = 0$, $\Delta D = 0$, $\boldsymbol{\eta}' = \mathbf{0}$, $\eta_{vol} = 0$

$\boldsymbol{\epsilon}^{ve}_n = (1 - D_n)\left(\boldsymbol{\epsilon}_n - \boldsymbol{\epsilon}^i_n\right)$, $E^{ve}_n = \boldsymbol{i} : \boldsymbol{\epsilon}^{ve}_n$, $\boldsymbol{e}^{ve}_n = \boldsymbol{\epsilon}^{ve}_n - \frac{1}{3}E^{ve}_n\boldsymbol{i}$, $\Delta E = \boldsymbol{i} : \Delta\boldsymbol{\epsilon}$, $\Delta\boldsymbol{e} = \Delta\boldsymbol{\epsilon} - \frac{1}{3}\Delta E\boldsymbol{i}$

repeat

$D_k = D_n + \Delta D$, $\boldsymbol{e}^i_k = \boldsymbol{e}^i_n + \Delta\lambda\boldsymbol{\eta}'$, $E^i_k = E^i_n + \Delta\lambda\eta_{vol}$, $\boldsymbol{e}^r_k = \boldsymbol{e}_{n+1} - \boldsymbol{e}^i_k$, $E^r_k = E_{n+1} - E^i_k$

$\boldsymbol{e}^{ve}_k = (1 - D_k)\,\boldsymbol{e}^r_k$, $E^{ve}_k = (1 - D_k)\,E^r_k$

$\sigma_{m(k)} = KE^{ve}_k$

call `Maxwell` $\longrightarrow \boldsymbol{S}_k$, $\boldsymbol{\xi}^{(j)}_k$, G^T

$\bar{\sigma} = \sqrt{\frac{3}{2}\boldsymbol{S}_k : \boldsymbol{S}_k}$, $\boldsymbol{\eta}' = \frac{3}{2\bar{\sigma}\sqrt{\frac{3}{2}+\frac{B^2}{3}}}\boldsymbol{S}_k$, $\eta_{vol} = \frac{B}{\sqrt{\frac{3}{2}+\frac{B^2}{3}}}$, $\hat{\sigma}^d = \frac{\bar{\sigma}+B^d\sigma_m}{1-D_k}$, $\hat{\sigma}^i = \frac{\bar{\sigma}+B^i\sigma_m}{1-D_k}$

call `evolve_damage` $\longrightarrow f^d$, τ^d, $\frac{\partial f^d}{\partial\hat{\sigma}^d}$, $\frac{\partial\tau^d}{\partial\Delta D}$

call `evolve_plastic` $\longrightarrow f^i$, τ^i, $\frac{\partial f^i}{\partial\hat{\sigma}^i}$, $\frac{\partial\tau^i}{\partial\Delta\lambda}$

$\Psi^d = \left\langle\frac{f^d}{\tau^d}\right\rangle^{n^d}$, $\Psi^i = \left\langle\frac{f^i}{\tau^i}\right\rangle^{n^i}$

$$\boldsymbol{E}_{rror} = \begin{bmatrix} \Delta\lambda - \Delta t\dot{\lambda}_0\Psi^i \\ \Delta D - \Delta t\dot{D}_0\Psi^d \end{bmatrix}, \quad \boldsymbol{J} = \begin{bmatrix} 1 - \Delta t\dot{\lambda}_0\frac{\partial\Psi^i}{\partial\Delta\lambda} & -\Delta t\dot{\lambda}_0\frac{\partial\Psi^i}{\partial\Delta D} \\ -\Delta t\dot{\lambda}_0\frac{\partial\Psi^d}{\partial\Delta\lambda} & 1 - \Delta t\dot{D}_0\frac{\partial\Psi^d}{\partial\Delta D} \end{bmatrix}$$

$$\begin{bmatrix} \Delta\lambda \\ \Delta D \end{bmatrix} = \begin{bmatrix} \Delta\lambda \\ \Delta D \end{bmatrix} - \boldsymbol{J}^{-1}\boldsymbol{E}_{rror}$$

until $\sqrt{\boldsymbol{E}_{rror} : \boldsymbol{E}_{rror}} < Tol \quad (k \leftarrow k + 1)$

update: $\boldsymbol{\sigma}_{n+1} = \boldsymbol{\sigma}_k + \sigma_{m(k)}\boldsymbol{i}$, $\boldsymbol{\xi}^{(j)}_{n+1} = \boldsymbol{\xi}^{(j)}_k$, $\boldsymbol{\epsilon}^i_{n+1} = \boldsymbol{e}^i_k + \frac{1}{3}E^i_k\boldsymbol{i}$, $D_{n+1} = D_k$

Output: $\boldsymbol{\sigma}_{n+1}$, $\boldsymbol{\epsilon}^i_{n+1}$, $\boldsymbol{\xi}^{(j)}_{n+1}$, D_{n+1}

For our particular set of evolution equations the derivatives needed in step 11 are

$$\frac{\partial \Psi^i}{\partial \Delta\lambda} = -n^i \Psi^i \left[\frac{1}{f^i} \frac{\partial f^i}{\partial \hat{\sigma}^i} \left(\frac{3G^T + B^i BK}{\sqrt{\frac{3}{2} + \frac{B^2}{3}}} \right) - \frac{1}{\tau^i} \frac{\partial \tau^i}{\partial \Delta\lambda} \right], \tag{2.21}$$

$$\frac{\partial \Psi^i}{\partial \Delta D} = -n^i \Psi^i \left[\frac{1}{f^i \left(1 - D\right)} \frac{\partial f^i}{\partial \hat{\sigma}^i} \left(\frac{3G^T}{\bar{\sigma}} \boldsymbol{S} : \boldsymbol{E}^r + B^i K E^r - \hat{\sigma}^i \right) \right], \tag{2.22}$$

$$\frac{\partial \Psi^d}{\partial \Delta\lambda} = -n^d \Psi^d \left[\frac{1}{f^d} \frac{\partial f^d}{\partial \hat{\sigma}^d} \left(\frac{3G^T + B^d BK}{\sqrt{\frac{3}{2} + \frac{B^2}{3}}} \right) \right], \text{ and} \tag{2.23}$$

$$\frac{\partial \Psi^d}{\partial \Delta D} = -n^d \Psi^d \left[\frac{1}{f^d \left(1 - D\right)} \frac{\partial f^d}{\partial \hat{\sigma}^d} \left(\frac{3G^T}{\bar{\sigma}} \boldsymbol{S} : \boldsymbol{e}^r + B^d K E^r - \hat{\sigma}^d \right) + \frac{1}{\tau^d} \frac{\partial \tau^d}{\partial \Delta D} \right]. \tag{2.24}$$

We note that though stress is evaluated using the Maxwell relations of Section 2.2 the iteration process makes use of the approximation

$$\Delta \boldsymbol{S} \approx 2G^T \left(1 - D_k\right) \left(\Delta \boldsymbol{e} - \Delta\lambda \boldsymbol{\eta}' \right) - 2G^T \Delta D \boldsymbol{e}^r \tag{2.25}$$

$$\Delta \sigma_m \approx K \left(1 - D_k\right) \left(\Delta E - \Delta \eta_{vol} \right) - K \Delta D E^r, \tag{2.26}$$

where G^T is the shear tangent stiffness that comes from Algorithm 1. The complete list of model parameters is listed in Table 2.1.

Table 2.1: Summary of model parameters

Variable	Description	Units
K	Elastic bulk modulus	FL^{-2}
G^{∞}	Long term elastic shear modulus	FL^{-2}
$G^{(j)}$	Viscoelastic shear moduli	FL^{-2}
$\tau^{(j)}$	Viscoelastic relaxation time constants	s
B^i	Inelastic rate function pressure proportionality constant	-
B^d	Damage rate function pressure proportionality constant	-
B	Inelastic flow pressure proportionality constant	-
m^i	Inelastic rate shape parameter	-
m^d	Damage rate shape parameter	-
n^i	Inelastic rate power coefficient	-
n^d	Damage rate power coefficient	-
τ_0^i	Initial inelastic viscosity	FL^{-2}
τ_L^i	Inelastic viscosity limit	FL^{-2}
τ_0^d	Initial damage viscosity	FL^{-2}
τ_L^d	Damage viscosity limit	FL^{-2}
λ_L	Equivalent inelastic strain at peak viscosity	-
D_L	Maximum damage	-
T_r	Reference temperature for TTS shift	T
c_0^{ve}	Viscoelastic WLF coefficient 1	-
c_1^{ve}	Viscoelastic WLF coefficient 2	T
c_0^i	Inelastic WLF coefficient 1	-
c_1^i	Inelastic WLF coefficient 2	T
c_0^d	Damage WLF coefficient 1	-
c_1^d	Damage WLF coefficient 2	T

2.7 Global Tangent Stiffness

The final set of equations necessary to implement this model into an implicit code is to define the tangent stiffness for the global stress-strain relationship. The tangent stiffness when there is no new inelastic strain or damage is

$$\frac{\partial \Delta \boldsymbol{\sigma}}{\partial \Delta \boldsymbol{\epsilon}} = (1-D)\left[2G^T\mathbb{I} + \left(K^- \frac{2G^T}{3}\right)\boldsymbol{i}\otimes\boldsymbol{i}\right], \tag{2.27}$$

which is simply an elastic stiffness matrix with the tangent shear and bulk moduli reduced by the damage. When the stress state is outside the zero evolution regions of the inelastic flow and damage surfaces the tangent stiffness should be further reduced to account for the change in damage and inelastic strain over the increment. However, at the time of this report we have only implemented the tangent stiffness above. This tangent stiffness will potentially result in slower convergence than a tangent stiffness that includes the other terms, but will not result in an inaccurate stress calculation.

2.8 Concluding Comments

The development of a viscoelastic-viscoplastic-viscodamage model has been documented in this chapter. The viscoelastic model is applied only to the shear response, while the viscoplastic and viscodamage models apply to both the shear and volumetric response. The viscoplastic and viscodamage evolution equations are aware of the triaxiality of the stress state. The experimental data that supports the choice of phenomena for this model as well as parameter estimation is covered in Chapter 3.

Chapter 3

Model Parameter Estimation

This chapter discusses the experimental data used to estimate the material parameters listed in Table 2.1 and the methods of fitting those parameters. First, the experimental data used for parameter estimation is discussed in Section 3.1. Then, the fitting procedures are discussed in Section 3.2.

3.1 Parameter estimation data

The model parameters are based entirely on a set of cyclic uniaxial experiments. Most of these experiments were documented in a 2013 report on PBX9501 behaviors [7]. A few additional experiments were performed in 2014, but they are the same format as those performed in 2013. The compressive and tensile experiments were performed using displacement control. An example of a compressive displacement schedule is shown in Figure 3.1. The crosshead was moved at a constant velocity to a desired displacement, then the crosshead was returned to the zero position at a rate an order of magnitude faster. At some point during that unloading the platen lost contact with the sample, which was then completely unloaded. Once the crosshead returned to its initial condition the sample was allowed to recover for approximately 2 hours. The process

was repeated with the same crosshead rates but a larger maximum crosshead displacement. After 10 to 20 cycles a final load to failure was performed.

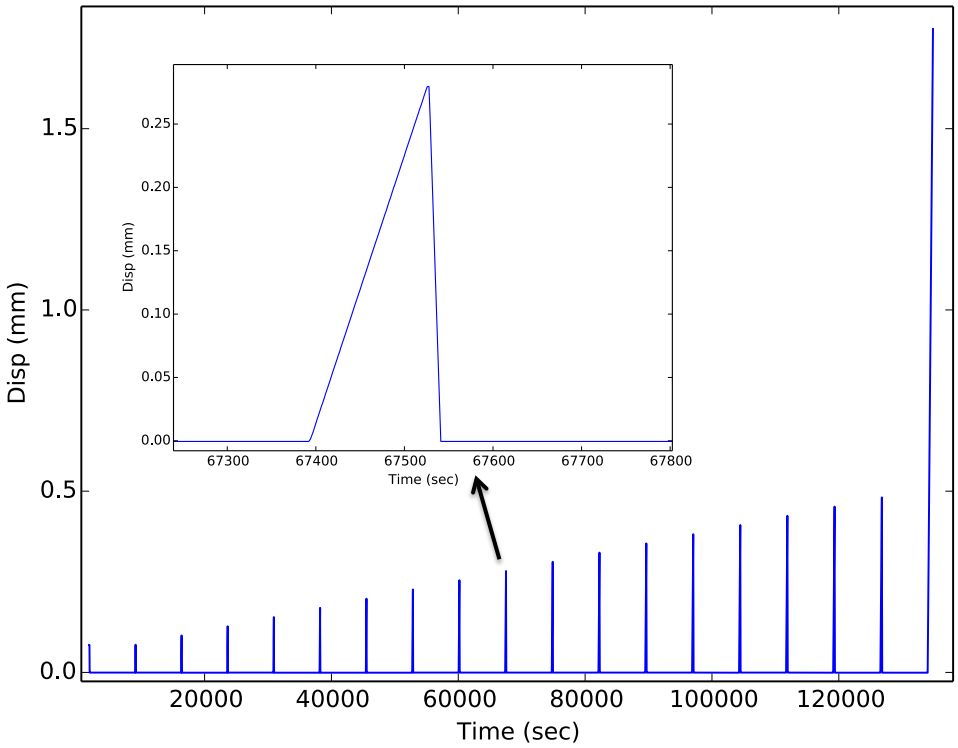

Figure 3.1: Typical crosshead displacement schedule

The experimental data set includes compression and tension experiments. The compression experiments were performed at strain rates ranging from ≈7x10^{-6} s^{-1} to ≈7x10^{-3} s^{-1}, and temperatures from -15 °C to 50 °C. There are also three compression experiments where 5 cycles with increasing displacements were performed followed by 4 cycles at a lower displacement. The purpose of these experiments was to explore the possibility of a growing threshold surface. The tension experiments were performed at ≈7x10^{-5} s^{-1} and 23 °C.

The displacement schedule shown in Figure 3.1 results in the engineering stress strain response shown in Figure 3.2. Changing loading slope, viscoelastic recovery, and permanent deformation can be observed in this experimental data. The viscoelastic recovery is evident in the difference between the strain at unload

and the strain at reload which occurs two hours later. In the subsequent cycle, the permanent deformation is evident in the nonzero strain at reload. This assumes that the material has fully recovered and that additional unloaded time would not result in a return to zero strain.

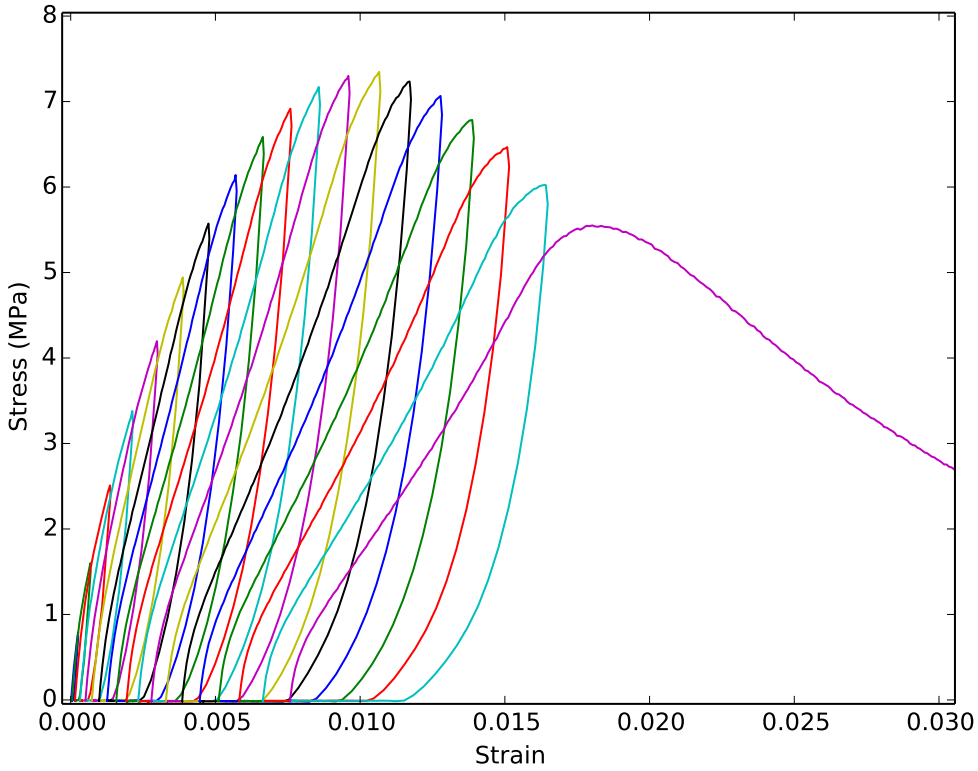

Figure 3.2: Typical response to cyclic compression

The time history of strain during the recovery period for a representative case is shown in Figure 3.3. This data represents the unloaded recovery for cycle five of the experimental data shown in Figure 3.2. In order to focus on the recovery, we plot data from 30 minutes into the recovery until the next cycle begins. An exponential decay function was fit to the unloaded recovery strain vs. time data and is shown in green on the figure. A relatively good fit is achieved for all the experimental data, though the fits are worse for cycles with a small strain relative to the characteristic noise in the measurements. The fit is used to

extrapolate ahead to a long time to approximate the permanent deformation given an infinite recovery period. In general, the strain determined by extrapolation is nearly the same as the strain at the end of the unloaded recovery. The strain at the end of the recovery for the example cycle is 0.2632% while the extrapolated strain is 0.2622%.

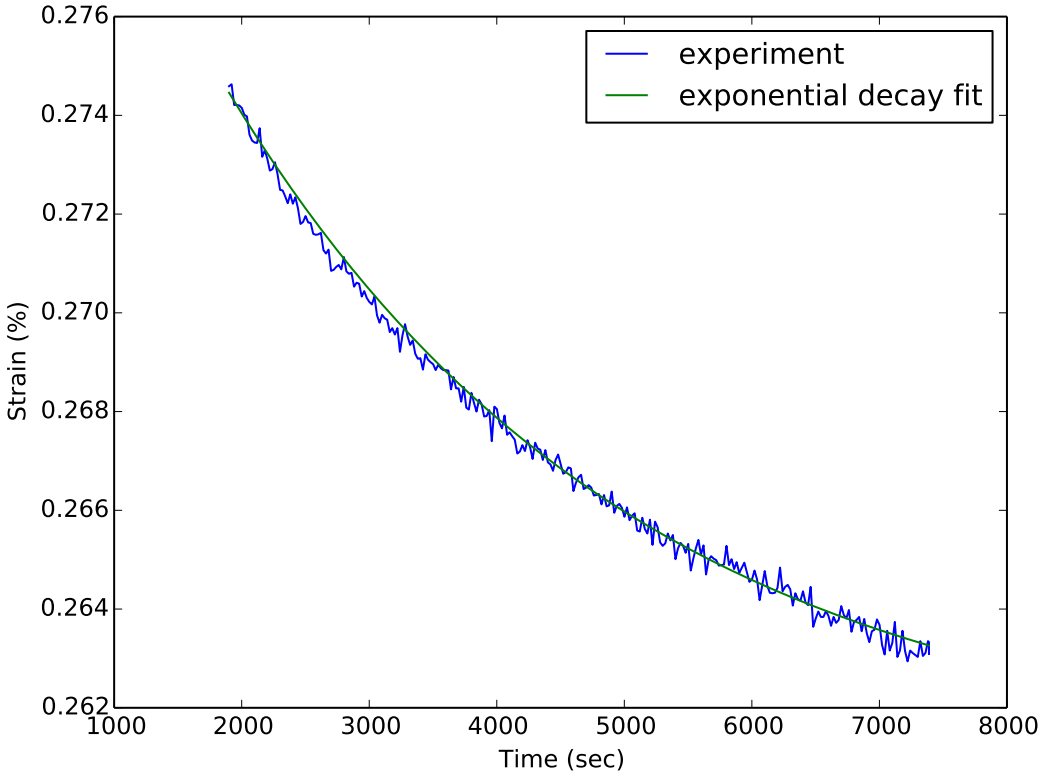

Figure 3.3: Unloaded recovery. Extrapolated strain is 0.2622%

The change in loading slope is more obvious in Figure 3.4 than in Figure 3.2. The figure only shows the loading portion of each cycle and toe corrections have been applied to shift the curves along the strain axis to intercept the origin. Each cycle clearly loads up a path that is more compliant than the previous cycle. Additionally, the maximum stress achieved in some of the later cycles is lower than for previous cycles. This may be a sign of softening, but all that can really be determined from this observation is that

the material stiffness has degraded enough to result in a smaller stress with a bigger strain.

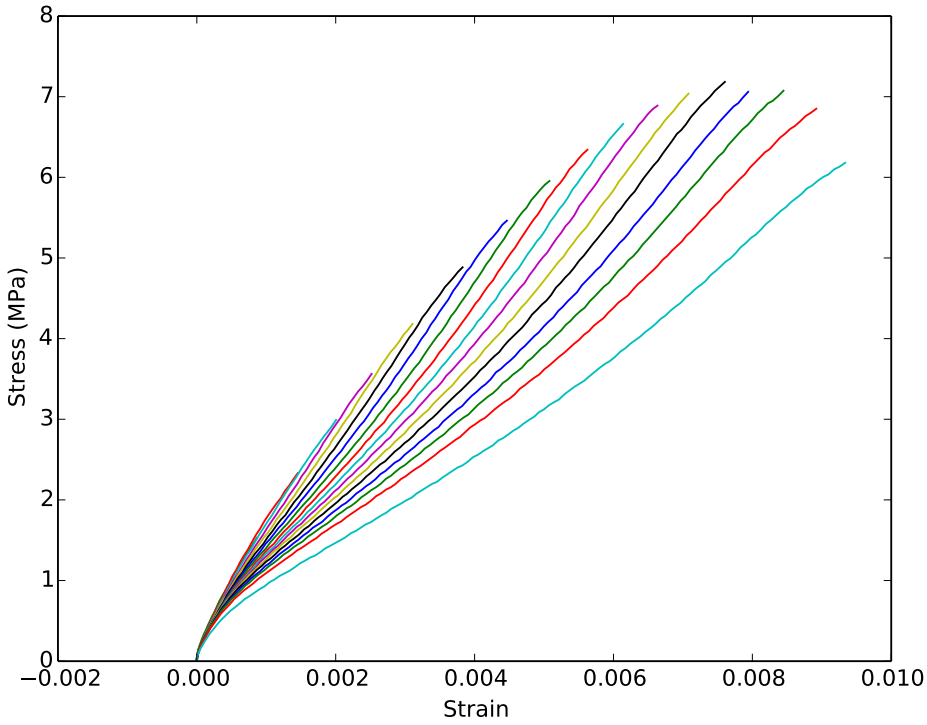

Figure 3.4: Stress-strain response under compressive loading shifted to zero initial strain

A measure of damage consistent with Equations 2.4 and 2.5 is shown in Figure 3.5. The recoverable strain (ϵ^r) is shown in blue and a scale factor (D) was used to scale the recoverable strain back to the viscoelastic (undamaged) strain. For each loading a single scale factor that minimizes the difference between the scaled stress-strain curve and that from the previous loading cycle is calculated. Then the cumulative scale factor from loading cycles prior to each cycle were calculated to determine the appropriate damage value for that particular loading cycle. For example, the damage factor for cycle three is the product of the scale factor which shifts cycle two back to cycle one and the scale factor which shifts cycle three back to cycle two.

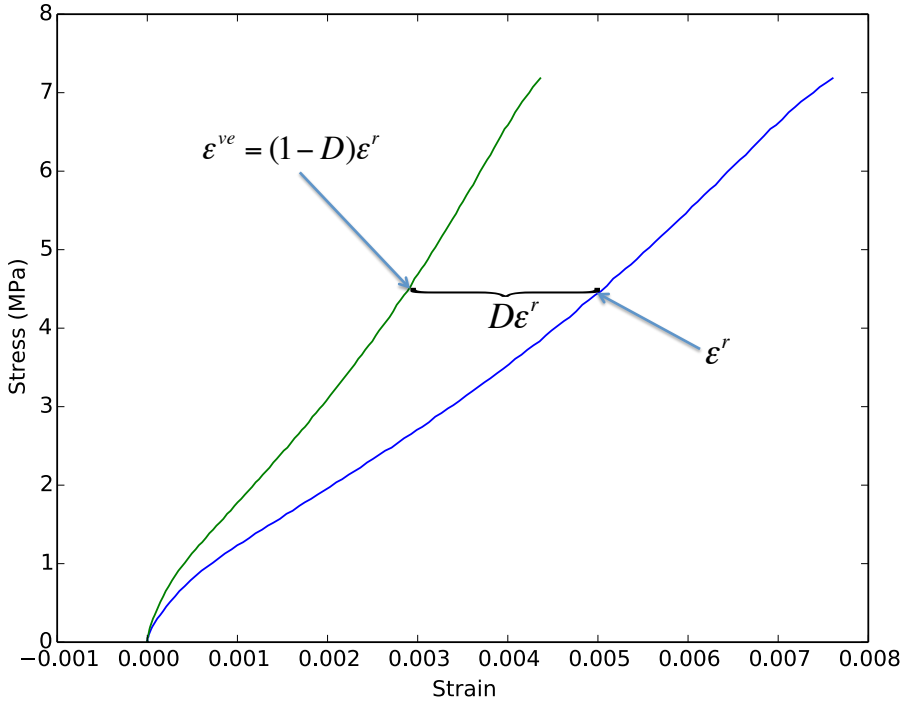

Figure 3.5: Example of damage scaled viscoelastic strain

All the loading curves from Figure 3.4 have been scaled using the damage variable. The scaled curves are shown in Figure 3.6. The curves essentially lie on top of each other except at the end of the loading cycle, where we speculate that the plastic evolution is becoming more significant than the damage. The agreement of the damage-scaled stress-strain curves during loading provides confidence that this method of determining the change in stiffness is appropriate.

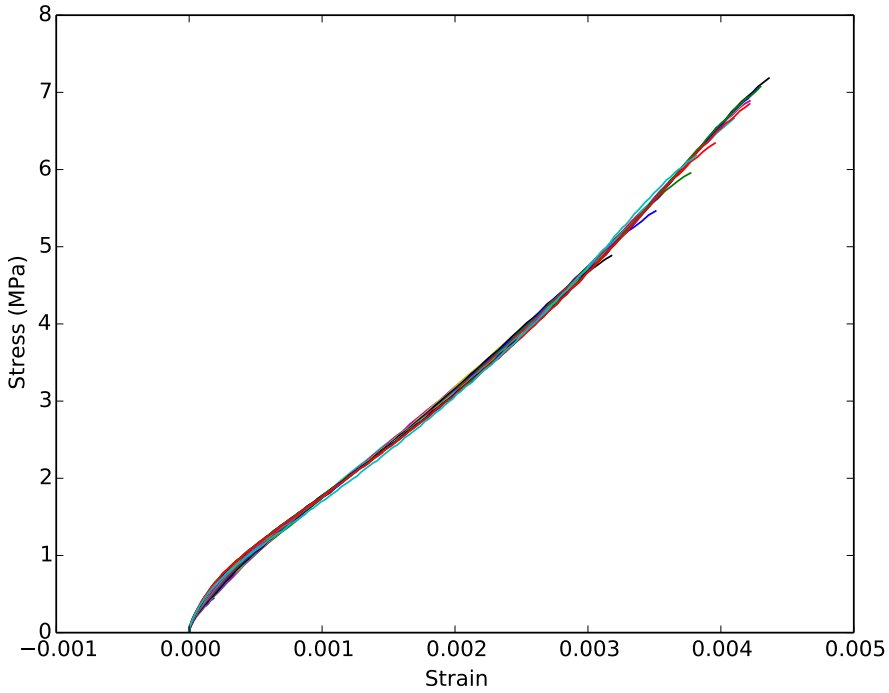

Figure 3.6: All load cycles scaled back to the undamaged loading curve

3.2 Parameter Estimation Procedures

The procedures for estimating inelastic strain and damage evolution parameters are discussed in this section. The experimental metrics used are the damage variable and axial residual strain measure as discussed in Section 3.1. The damage evolution described by Equation 2.12 as discussed in Chapter 2.3 is dependent on the state of stress and the current damage state, while the inelastic strain evolution described by Equation 2.14 as discussed in Chapter 2.4 is dependent on the stress and the inelastic strain history, as well as current damage state so we must begin by fitting the damage evolution parameters, prior to fitting of the inelastic strain evolution parameters.

The ideal approach to fitting the damage evolution parameters is to iterate on the parametric values until a residual is minimized. The residual is calculated by numerically integrating Equation 2.12 given the

measured stress-time data and a trial set of parameter values (see Algorithm 2 for a list) then calculating the difference between the predicted damage and the measured damage.

Much effort went into developing the numerical integration scheme. We began with a 4^{th} order Runge-Kutta integration [3]. Results using the 4^{th} order scheme were highly sensitive to the sampling rate, so we incorporated a sub cycling Runge-Kutta 3-2 method. The Runge-Kutta 3-2 method provides 3^{rd} order accuracy and an estimate of the ideal step size given a desired maximum error [1]. This method was accurate, but required many cutbacks in step sizes so we finally incorporated a sub-cycling implicit method. This method consists of two subroutines. The first subroutine is a single step Newton-Raphson iterative implicit integration [3] as described in Algorithm 5. In addition to the parameters, this algorithm takes in an initial damage value, time step, and the appropriate effective stress at the end of that time step. The initial damage is zero for the first cycle and for all other cycles has been determined through integration of the previous cycle. The algorithm returns the damage at the end of the time step and a recommended step size. The recommended step size will be the input step size if convergence was reached otherwise it will be 25% of the input step size. The input variable, $\dot{D}_0$, is a function of temperature and, consequently is a constant for any particular isothermal experiment.

Algorithm 5 Integrate $\dot{D}$

Input: VARS : D_n, Δt, $\hat{\sigma}_{n+1}$, $\dot{D}_0$ PARAMS : m^d, n^d, D_L, τ_0^d, τ_L^d

initialize: $k \leftarrow 0$, $\Delta D = 0$, $k = 0$
repeat
  $D_k = D_n + \Delta D$
  $E_{rror} = \Delta D - \dot{D}_0 \Delta t \left\langle \frac{f^d(\hat{\sigma}_{n+1})}{\tau^d(D)} \right\rangle^{n^d}$
  $J = \Delta t n^d \left\langle \frac{f^d}{\tau^d} \right\rangle^{n^d - 1} \frac{1}{\tau^d} \left[\frac{\partial f^d}{\partial D} - \frac{f^d}{\tau^d} \frac{\partial \tau^d}{\partial D} \right]$
  $\Delta D = \Delta D - J^{-1} E_{rror}$
  $k = k + 1$
until $E_{rror} < tol$ or $k > max\_iters$
if $E_{rror} > tol$ **then**
  $\Delta t_{rec} = 0.25 \Delta t$
else
  $\Delta t_{rec} = \Delta t$
end if
update: $D_{n+1} = D_k$

Output: D_{n+1}, Δt_{rec}

The actual integration over an increment may be done in multiple steps, if damage is changing quickly, using the subroutine described in Algorithm 6. This algorithm assumes a linear change in stress with time, which allows an evaluation of Algorithm 5 at sub-increments. It will continue to increment the damage until the total time step is reached. This algorithm converged quickly and is computationally efficient enough to allow us to calculate errors over all the data sets with an acceptable damage tolerance of tol=1x10^{-4}.

Several cost functions and optimization algorithms were employed, but none achieved a desirable comparison of experiments and predictions. In the end a manual optimization, approximating a bisection method, was performed. This was more successful than the attempted automated methods, because the human brain is able to quickly recognize local minima and compensate resulting in a better fit. In the future other automation methods, genetic algorithms for instance, will be investigated.

Algorithm 6 Integrate $\dot{D}$ multistep

Input: VARS : D_n, Δt, $\hat{\sigma}_n$, $\hat{\sigma}_{n+1}$, $\dot{D}_0$ PARAMS : m^d, n^d, D_L, τ_0^d, τ_L^d

initialize: $\Delta t_{complete} = 0$, $\Delta t_{try} = \Delta t$, $\hat{\sigma}_k = \hat{\sigma}_n$, $D_k = D_n$

$\frac{d\sigma}{dt} = \frac{\hat{\sigma}_2 - \hat{\sigma}_1}{\Delta t}$

repeat

  $\hat{\sigma}_{k+1} = \hat{\sigma}_k + \frac{d\sigma}{dt}\Delta t_{try}$

  call Integrate $\dot{D} \longrightarrow D_{k+1}$, Δt_{rec}

  if $\Delta t_{rec} \geq \Delta t_{try}$ **then**

    $\Delta t_{complete} = \Delta t_{complete} + \Delta t_{try}$, $\hat{\sigma}_k = \hat{\sigma}_{k+1}$, $D_k = D_{k+1}$

  else

    $\Delta t_{try} = \Delta t_{rec}$

  end if

  if $\Delta t - \Delta t_{complete} < \Delta t_{rec}$ **then**

    $\Delta t_{rec} = \Delta t - \Delta t_{complete}$

  end if

until $\Delta t_{complete} = \Delta t$

update: $D_{n+1} = D_k$

Output: D_{n+1}

First, we optimized the parameters for all the cyclic data collected at 23 °C including both tension and compression. We chose 23 °C as the reference temperature because over 50% of our data was collected at that temperature. The value of $\dot{D}_0$ is set at 1.0 for the 23 °C experiments. A plot of predicted damage level vs. experimentally estimated damage level is shown in Figure 3.7. Overall, the fits are reasonably good, though they are noticeably worse at lower damage levels. One experiment that was not included in the fitting process is a creep experiment. In this creep experiment, performed by Darla Thompson (WX-7), the material was exercised in a slightly different manner. The experiment included only four cycles, and rather than unloading immediately the load was held for a relatively long time (30 min for the first cycle and monotonically increasing to 8 hours for the final cycle). The damage measured in the creep experiment is also not well captured in the predictions, but as noted above, this creep experiment

is relatively new and was not included in the fitting. We note that the measured damage is much smaller for the tension experiments than for the compression. Because tensile experiments fail nearly immediately after the peak is achieved the experiments cannot endure additional loading cycles including large amounts of damage. This could be the result of a different damage mechanism for compression and tension, which is not captured by this modeling effort. Additional testing is planned for FY15 to help understand the different damage mechanisms in tension and compression.

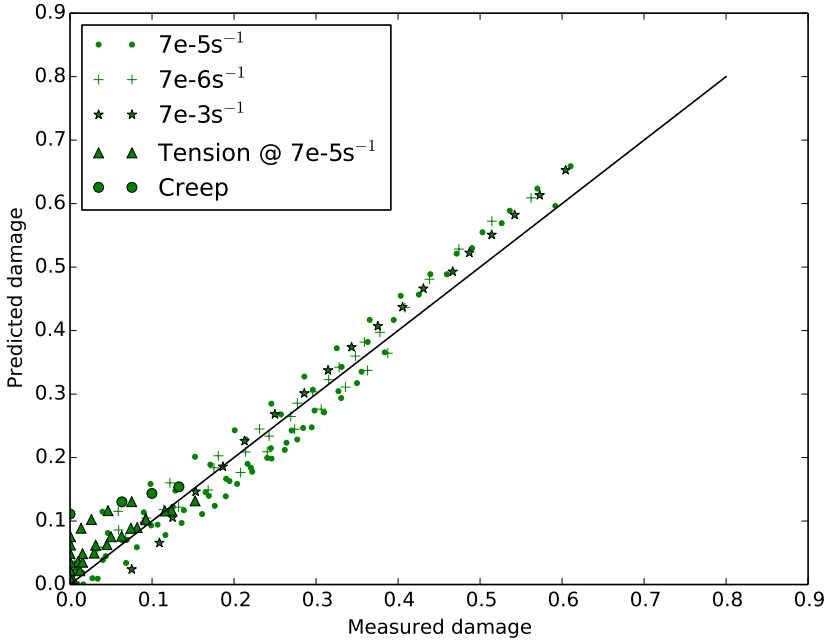

Figure 3.7: Predicted damage vs. experimentally estimated damage

Next, we hold the parameters fixed and optimize the value of $\dot{D}_0$ for experiments at -15 °C and 50 °C. These optimal values are then fit to the WLF-like function described in Equation 2.16. The predicted damage vs. experimentally estimated damage is plotted in Figure 3.8. A reasonable fit is achieved for temperatures of -15 °C, and 50 °C.

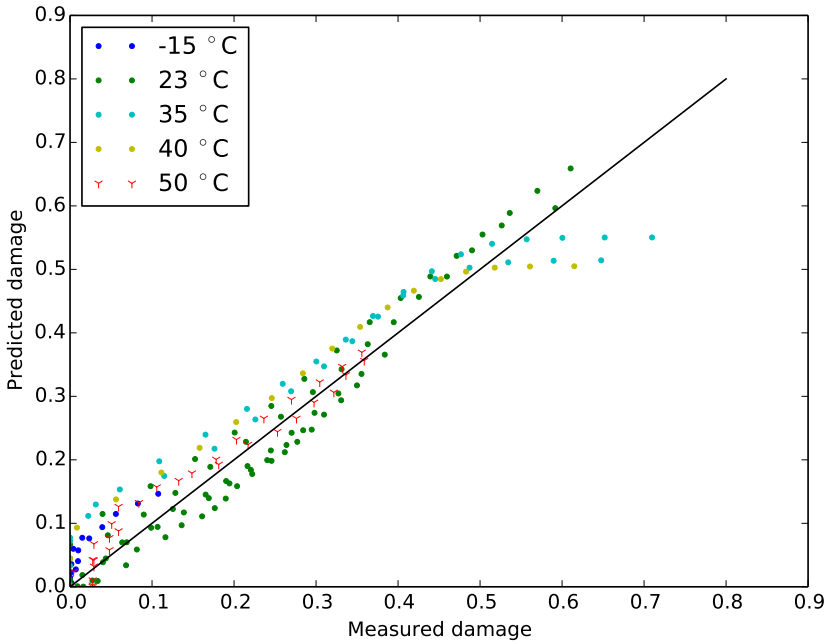

Figure 3.8: Damage predictions with TTS shift applied.

Having developed a reasonable set of parameters for damage evolution the damage can be evaluated for every data point in the experiments. This is necessary as a first step to fitting the inelastic strain evolution because of the dependence on D in Equation 2.14. The inelastic strain evolution is in terms of λ, but we measure the inelastic strain in the direction of the applied load as shown in Figure 3.9. In the diagram the flow is in the direction of the green arrows. Results from experiments to date only include strain in the direction of loading, which is shown in the red lines, one for tension and one for compression. The dashed lines show the projection of the actual (assuming associative flow) inelastic flow onto the loading directions. This projection is the only component of strain that has been measured. Consequently, to identify the flow direction and uniquely determine B from uniaxial experiments, a scheme utilizing both tension and compression data has been developed.

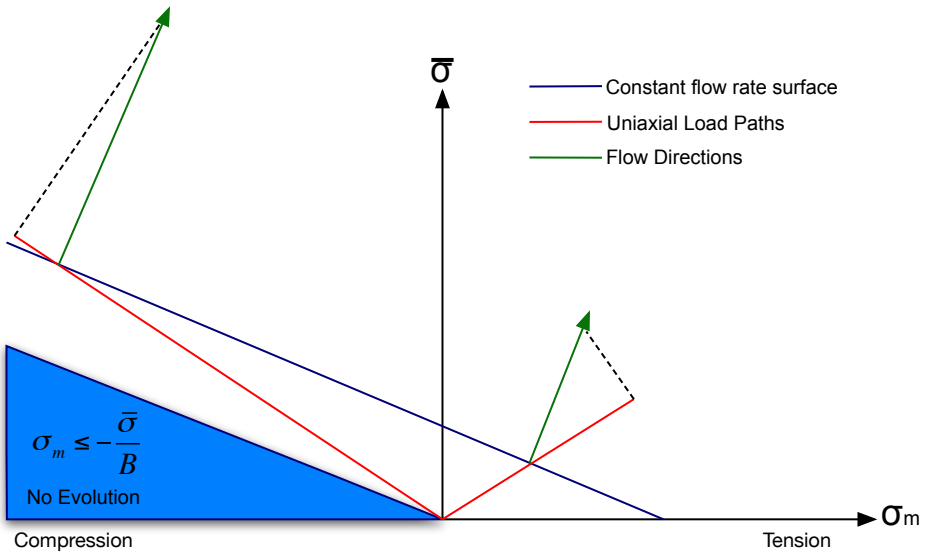

Figure 3.9: Diagram of of the difference between inelastic flow and measured inelastic strain

To fit Equation 2.14, we evaluate the inelastic strain under uniaxial tension and uniaxial compression conditions. Let uniaxial loading be aligned in the x direction. The inelastic strain rate in that direction is evaluated from Equations 2.14 and 2.15 as

$$\dot{\epsilon}^i_{11} = \dot{\lambda}\left[\frac{3}{2\bar{\sigma}\sqrt{\frac{3}{2}+\frac{B^2}{3}}}S_{11} + \frac{B}{3\sqrt{\frac{3}{2}+\frac{B^2}{3}}}\right], \tag{3.1}$$

where $S_{11} = \frac{2}{3}\bar{\sigma}$ in uniaxial tension, and $S_{11} = -\frac{2}{3}\bar{\sigma}$ in uniaxial compression. The scale factor, $m\left(S_{11}\right)$ is defined as

$$m\left(S_{11}\right) = \frac{3+B}{3\sqrt{\frac{3}{2}+\frac{B^2}{3}}}, \tag{3.2}$$

for $S_1 1 > 0$, and

$$m\left(S_{11}\right) = \dot{\lambda}\frac{-3+B}{3\sqrt{\frac{3}{2}+\frac{B^2}{3}}} \tag{3.3}$$

for $S_{11} < 0$.

Fitting of parameters in Equation 2.14 is conducted by scaling measured ϵ_{11} data to obtain an effective λ as $\dot{\lambda} = \frac{1}{m}\dot{\epsilon}_{11}$. The algorithms used to integrate the inelastic strain rate are the same as Algorithms 5 and

6 and, therefore, will not be repeated here. Again, automated optimization resulted in less than satisfactory predictions, so a manual optimization process was carried out. The resulting predicted inelastic strain is plotted against the experimentally estimated residual strain in Figure 3.10. The figure contains data and predictions for many experiments carried out at 23 °C. We achieved a fit with errors of less than 10% for cycles where the residual strain is less than 0.5%.

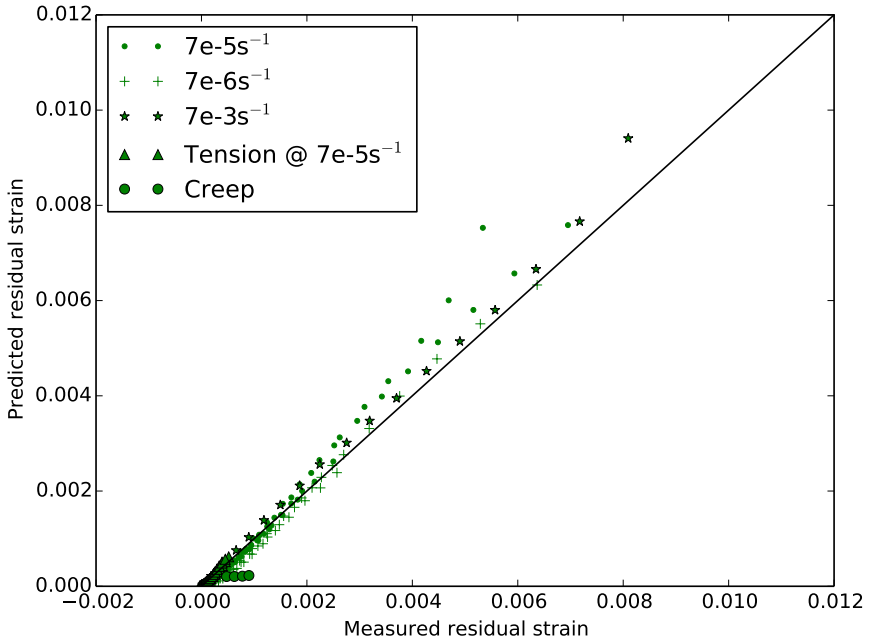

Figure 3.10: Predicated axial inelastic strain vs. experimentally estimated axial inelastic strain

Temperature dependence of the inelastic strain evolution is also handled through time-temperature-superposition. Having optimized the evolution parameters against 23 °C data we determine the optimal $\dot{\lambda}_0$ necessary to fit the -15 °C, and 50 °C experimental data. Three temperatures are shown in Figure 3.11. The fit of inelastic strain evolution at different temperatures is not as good as the evolution of the damage at those temperatures, but the major divergence at temperatures other than 23 C°C occurs for a residual strain greater than 0.5%.

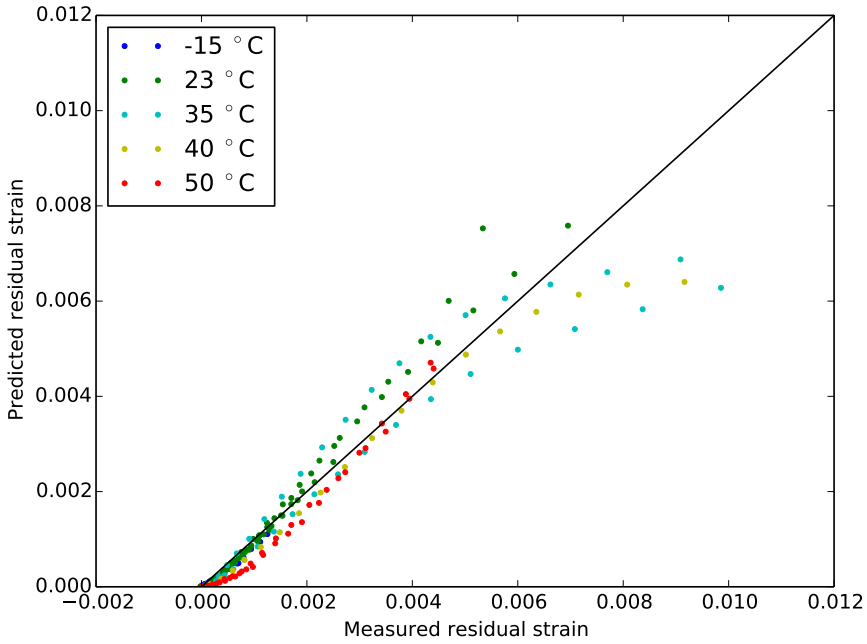

Figure 3.11: Inelastic strain predictions with TTS shift applied

3.3 Conclusions

Overall, there is some room for improvement of the evolution laws or their associated parameters to better fit the broad range of experimental data, but the inclusion of both inelastic strain and damage phenomena along with the achieved fits to experimental data greatly improve our predictive capability under cyclic loading of this material. These improvements are demonstrated in Chapter 4.

Chapter 4

Validation

At this time the validation evidence is limited to monotonic uniaxial experiments and some features of the cyclic experiments. The monotonic experiments were not used for model fitting so these are good validation experiments. The change in slope and the permanent strain were extracted from the cyclic experiments and used for fitting as discussed in Chapter 3, but the peak stress from each cycle and the strain immediately after unload were not used for fitting. We will use a measure (to be defined later) of slope and the total strain at peak stress for the monotonic experiments as well as the cycle peak stress and unloaded strain from the cyclic experiments as our validation evidence. To demonstrate the improvements in predictive capability resulting from this modeling effort, we will also compare the legacy viscoelastic material model to the experimental data.

The simulations and comparisons to experimental data were performed using an automated system developed under the ASC Engineering V&V project. The Validation Test Suite (eventually to be the Verification and Validation Test Suite) includes pre-packaged simulations of experiments along with associated experimental data. The suite runs the simulations, extracts the metrics of interest, and creates plots and

tables for inclusion in reports. Currently, the suite includes experiments for PBX9501, Sylgard 184, and S5370, but will be extended to include numerous other models in the future. For further information or access to the suite see Ted Lyman (W-13) or the documentation [14].

4.1 Performance of the model for simulations of monotonic experiments

Stress-strain data and simulations for monotonic tension and compression experiments are shown in Figures 4.1, and 4.2 respectively. We can see reasonable match between the simulation and the experiment, though the tension simulations reach peaks that are much higher than the experiments.

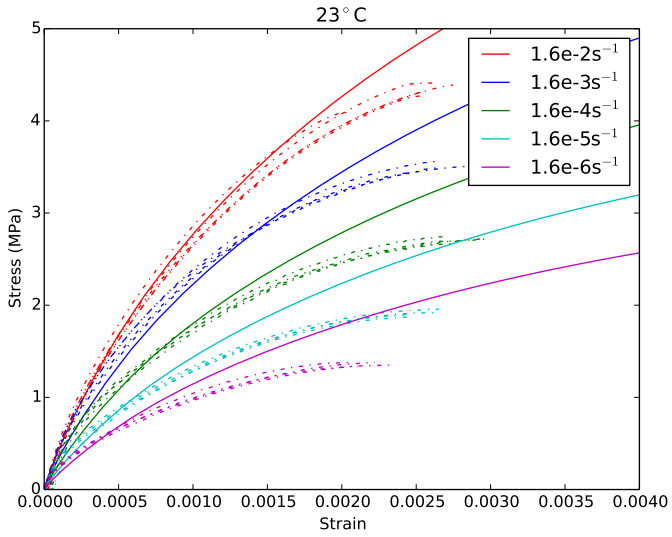

Figure 4.1: Monotonic tension experiments (dashed lines) and simulations (solid lines)

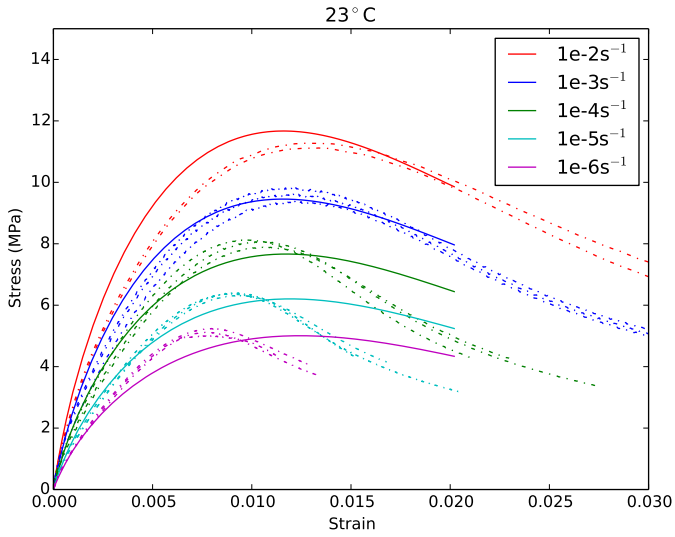

Figure 4.2: Monotonic compression experiments (dashed lines) and simulations (solid lines)

A quantifiable measure of the performance is preferable to the qualitative statement of the previous paragraph so we analyzed two metrics. We also want to be able to apply these metrics to the legacy viscoelastic material model used in W-13 so we can demonstrate improvements in predictive accuracy, or lack there of, provided by this model. First, we define a measure of the *early slope* as the slope of the best

fit straight line between 10% and 40% of the peak stress. Next, we look at the experimental peak stress. The legacy viscoelastic material model does not exhibit a peak in the stress-strain response so we define the response of interest as the stress at the strain for which the experiment reaches a peak stress. Both metrics are indicated an example experimental response in Figure 4.3.

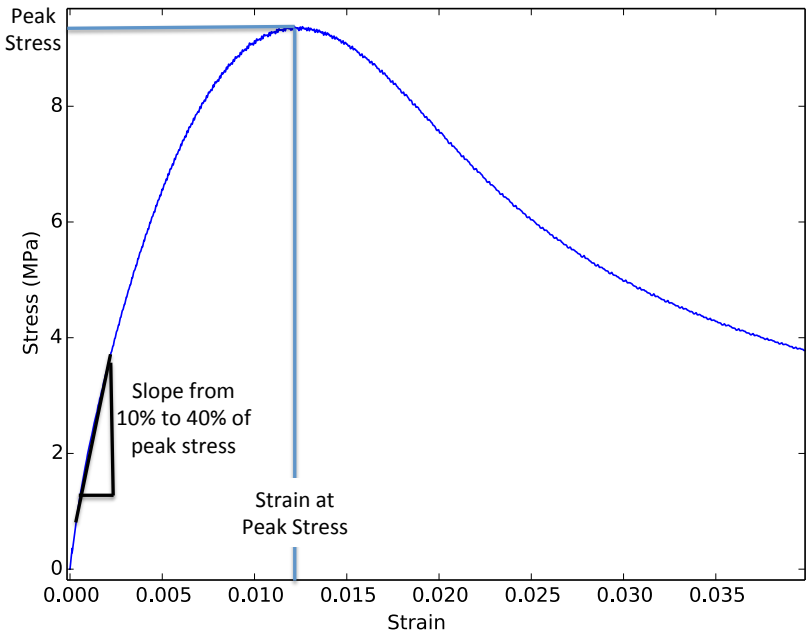

Figure 4.3: Performance metrics for model under monotonic uniaxial loading

The quantified metrics for uniaxial compression are summarized in Table 4.1. The table includes the metrics for this model ($VPVD$) as well as the quantified metrics for the legacy viscoelastic model. For more information on the legacy model see [16]. The better results are shown in green while the worse results are shown in red. Overall, the legacy viscoelastic model exhibits a better early slope than the new model, but the stresses predicted at the strain associated with the experimental peak stress are much closer for the new model than for the legacy model.

Table 4.1: Summary of results from compression comparisons.

Rate (s-1)	Temp C	VPVD		Viscoelastic	
		Slope Error (%)	Peak Error (%)	Slope Error (%)	Peak Error (%)
1.0E-02	23	30.97	3.42	15.6	131.8
1.0E-03	23	34.83	-1.72	13.2	101.3
1.0E-04	23	19.65	-5.07	2.9	64.6
1.0E-04	23	17.78	-5.54	1.3	48.7
1.0E-06	23	6.55	-10.23	-13.3	26.6
1.0E-03	0	26.7	10.06	12.4	143.1
1.0E-05	0	19.77	-5.45	-0.8	92.5
1.0E-03	50	37.16	-6.08	25.8	74.0
1.0E-05	50	23.91	-2.44	10.0	51.8

The monotonic tension performance metrics are summarized in Table 4.2. Again, there are a few experiments where the legacy viscoelastic model performed better with respect to the early slope metric, but the new model consistently provided a better prediction of the stress associated with the experimental strain at peak stress.

Table 4.2: Summary of results from tension comparisons.

Rate (s-1)	Temp C	VPVD		Viscoelastic	
		Slope Error (%)	Peak Error (%)	Slope Error (%)	Peak Error (%)
1.6E-02	23	0.9	13.1	-13.0	46.4
1.6E-03	23	-9.1	18.9	-25.9	44.0
1.6E-04	23	1.4	27.4	-19.7	60.7
1.6E-05	23	11.9	34.1	-9.8	63.4
1.6E-06	23	14.8	39.6	-12.0	54.9
1.6E-03	0	-17.1	6.6	-30.0	26.8
1.6E-05	0	-12.3	31.2	-25.0	54.6
1.6E-03	50	32.9	38.4	17.6	107.8
1.6E-05	50	193.8	138.1	127.9	226.9

Overall, the new model performs well though there is room for improvement. The early slope estimates are commonly not as good as those predicted by the legacy viscoelastic model, though it should be noted that the legacy model was fit to this monotonic experimental data whereas the new model was not. Alternatively, the new model can better predict the softening as is evident in the peak stress predictions which are, across the board, better than the predictions made using the legacy model.

4.2 Performance of the model for simulations of cyclic experiments

We have only performed the comparisons between predictions and cyclic uniaxial compression experiments at this time, because the tension experiments were slightly more complicated and require an additional user subroutine to be developed and implemented in the Validation Test Suite [14]. These updates are expected early in FY15. Examples of the stress-strain data for an experiment compared to the new model and to the legacy model are shown in Figures 4.4, and 4.5 respectively. It is clear that for this example the new model outperforms the legacy model.

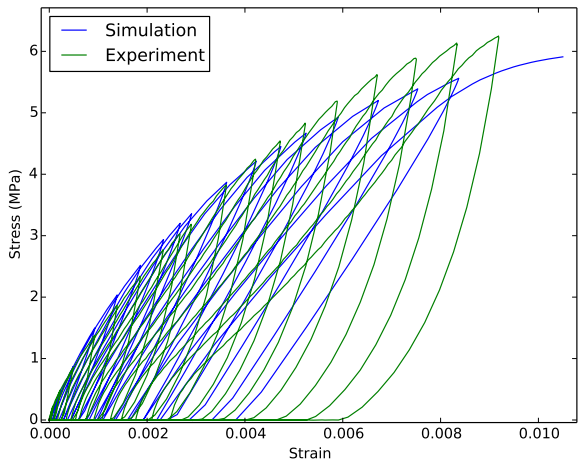

Figure 4.4: Cyclic stress-strain comparisons for VPVD at 23 C° and 0.0005 in/min

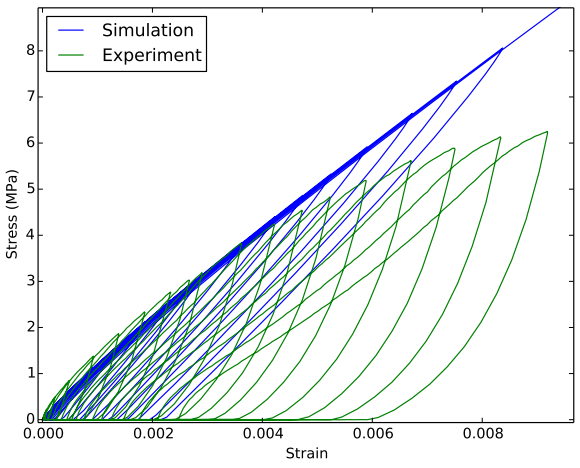

Figure 4.5: Cyclic stress-strain comparisons for legacy model at 23 C° and 0.0005 in/min

It would be cumbersome to evaluate plots such as those shown in Figures 4.4, and 4.5 for all experimental configurations so we will evaluate several metrics individually. The metrics are shown in Figure 4.6. The first metric is the peak stress for each cycle. The second metric is the unloaded strain for each cycle. This is the strain immediately after the load returns to zero for each cycle. Finally, we will look at the strain at the end of each recovery period. This is actually not a good validation metric for the new model because it is very close to the inelastic strain used for fitting the model. However, it will be used to demonstrate improved predictive capability over the legacy viscoelastic model.

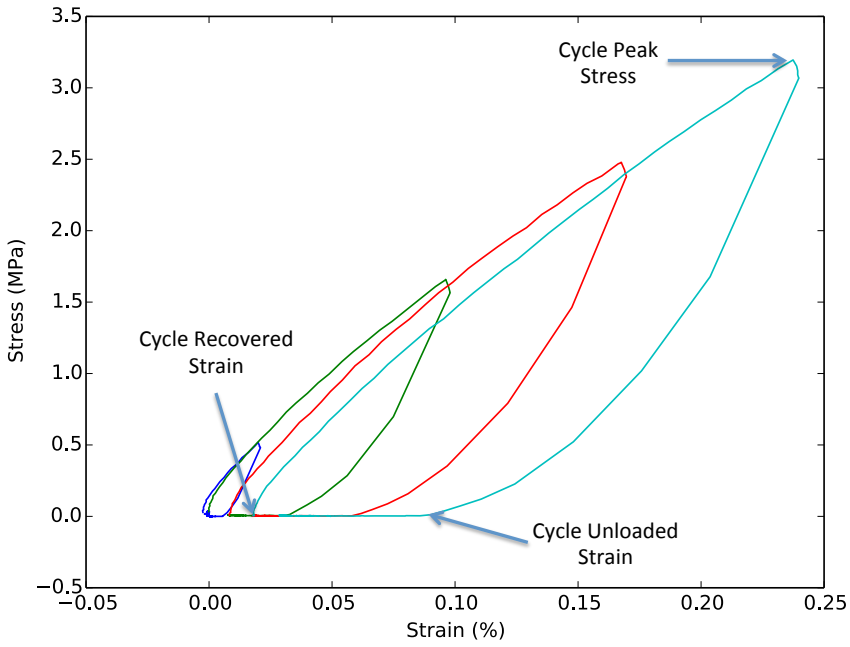

Figure 4.6: Performance metrics for model under cyclic uniaxial loading

The peak stresses for each cycle predicted by the new model (+) and the legacy model (dots) are plotted against measurements and shown in Figure 4.7. The data plotted includes all the cyclic compression experiments performed in FY13 and FY14. The black line represents a straight line with a slope of 1.0, which means points falling on the line have predictions equal to the measurement. Deviation from the line

is error. The new model clearly stays closer to the line than the viscoelastic model, especially for cycles at higher stresses. The extreme curvature of some of the legacy model predictions is because the measured peak stresses were beginning to fall while the legacy model always predicts a higher stress for a higher strain. The improved results when using the new model come as no surprise because improved response under cyclic loading was one of the main drivers for this model development, but it is clear evidence of the improved predictive accuracy achieved.

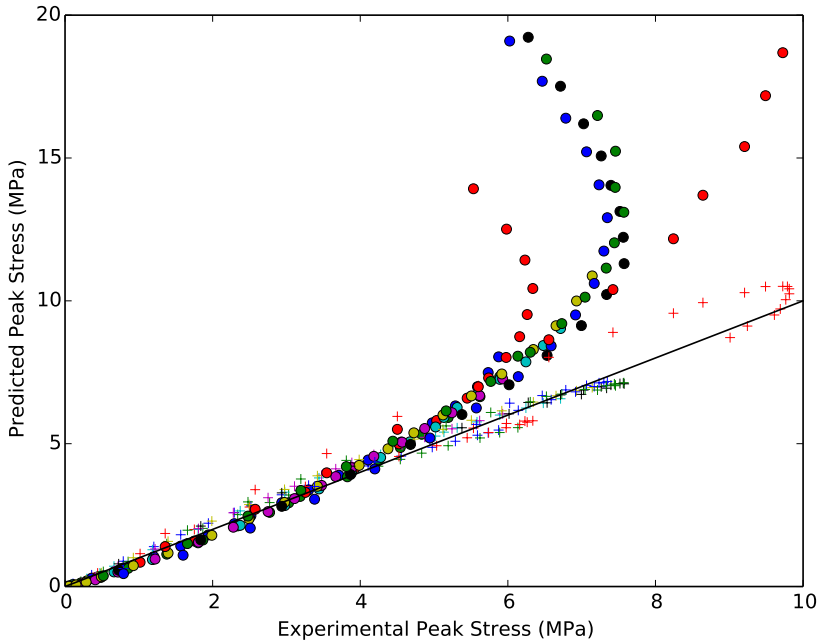

Figure 4.7: Predicted peak stress vs. measured peak stress. Legacy simulations are plotted with dots. The new model is plotted with + symbols.

The predicted strain at unload vs. the measurements are shown in Figure 4.8. Again, the black line indicates a perfect fit while the dots are the predictions for each cycle made with the legacy model and the plus symbols indicate the predictions using the new model. The new model performs significantly better. On average, the new model slightly underpredicts the strain at unload, while the legacy viscoelastic model

greatly underpredicts the strain at unload. In both cases better results could be achieved if unloading response were included in the fitting of the viscoelastic models, but these results are encouraging.

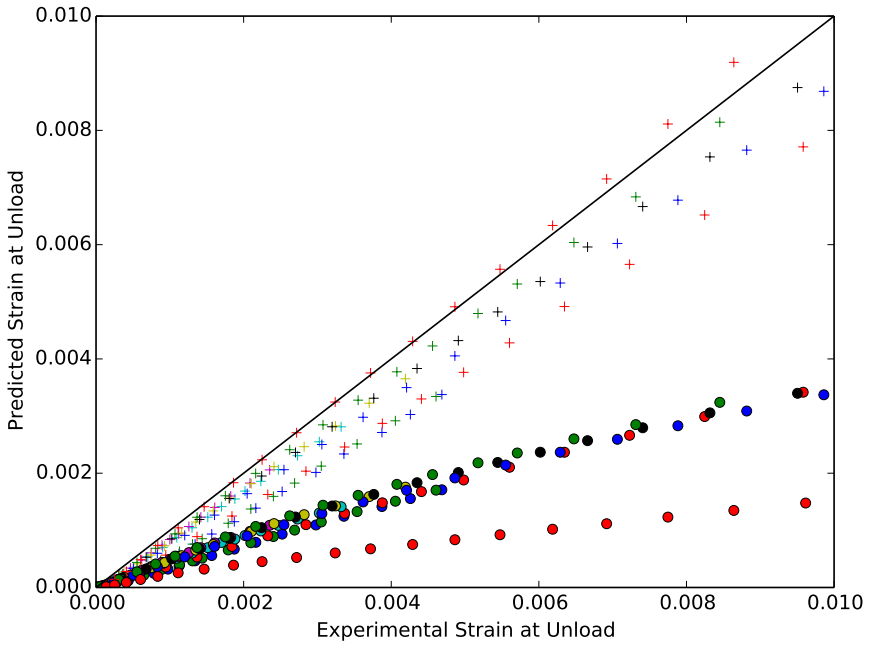

Figure 4.8: Predicted peak stress vs. measured peak stress. Legacy simulations are plotted with dots. The new model is plotted with + symbols.

Finally, we compare the predicted strain after recovery. These results are shown in Figure 4.9. The legacy model results plotted with dots are below the measurements. In fact, in many cases the strain after recovery predicted by the viscoelastic model is zero. It is expected that given sufficient time the legacy model would return to zero strain, while the new model will not. The new model predictions are quite good. On average, the new model does predict the measurements. This is certainly not surprising because experimentally, the estimated inelastic strain was not much different from the strain after the recovery period, and the estimated inelastic strain was used as a fitting parameter, as discussed in Chapter 3.

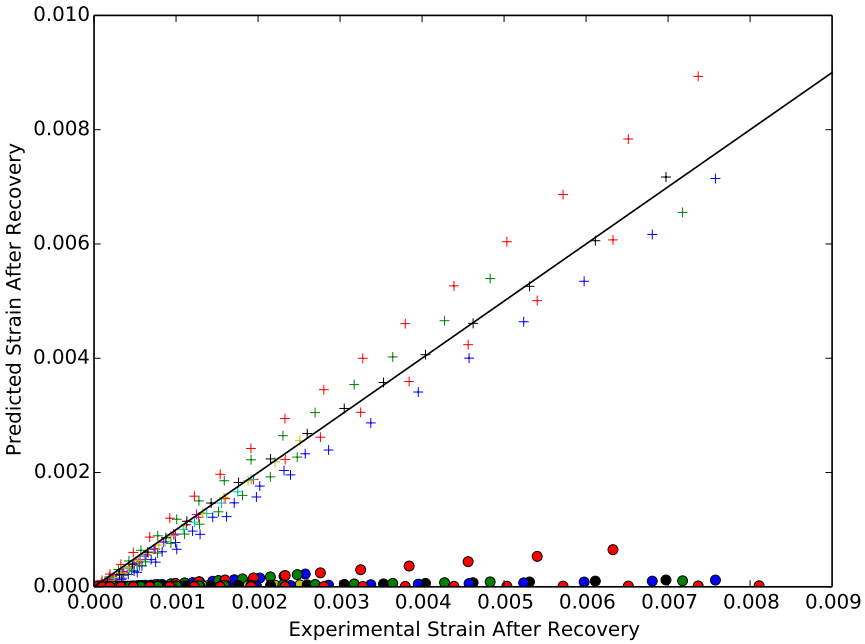

Figure 4.9: Predicted peak stress vs. measured peak stress. Legacy simulations are plotted with dots. The new model is plotted with + symbols.

4.3 Validation Conclusions

Overall, the new model does perform very well with respect to the validation evidence shown in this chapter. The new model is clearly a significant improvement over the legacy viscoelastic model, but we need to include many more small scale and component level validation experiments in the suite used for PBX9501. There are a few experiments which were performed on geometries not appropriate for this report and at least one experiment planned for FY15 (see Section 5.1 for details).

Chapter 5

Conclusions

This report documents the development of a constitutive model for PBX9501. The constitutive model includes viscoelastic, viscoplastic, and viscodamage behaviors. This model improves the predictive capability of simulations performed by W-13 that include PBX9501 components. The legacy model used for simulations of these components is a simple viscoelastic model and we showed, in Chapter 4, that the new model greatly improves predictions for response to cyclic loading. That improvement does come at the cost of some accuracy for monotonic loading, but further experiments to be discussed later in this chapter may provide missing knowledge enabling better fit over both loading regimes.

5.1 Future Experiments

There is a considerable experimental program planned for FY15 in support of continued development of this constitutive model. These experiments include cyclic experiments similar to those discussed in Chapter 3, cyclic creep experiments, an exploratory experiment, and a validation experiment.

The cyclic experiments conducted in FY15 will be similar to those conducted in FY14, but with

additional diagnostics to provide simultaneous measurement of axial and radial strain in the sample. The additional diagnostics support the estimation of the inelastic flow pressure proportionality constant, B, as discussed in Chapter 3.2. These experiments might also provide additional information regarding the splitting of the shear and volumetric parts of the stiffness as well as their degradation (damage).

Darla Thompson (WX-7) plans to perform a series of cyclic creep experiments in FY15, which will include the additional diagnostics discussed above and will be conducted at a variety of temperatures and loads. These experiments will extend the applicable range of the model and give a better indication of the form of the denominator for the damage and inelastic strain evolution equations.

An exploratory experiment planned by Darla Thompson will provide insight into the potential anisotropic nature of the damage. The plan is to test cubes of HE under cyclic compressive loading. Some of the samples will be cycled to failure. Other samples will be cycled, but the cycles will be interrupted before failure. Then the samples will be turned 90° and loading is resumed perpendicular to the previous cycles. We might observe differences between the behavior of these two sample sets which would indicate a significant anisotropic component to the damage. Hopefully, we will be able to identify a region (magnitude of damage) where the isotropic assumptions made in this model development are valid.

Cheng Liu (MST-8) is developing an experiment which will put the center of a thin disk in a near biaxial tensile state. This experiment will not achieve a uniform stress state so we do not consider it a parameter estimation experiment, but it will provide good validation evidence in a stress state that is relevant and interesting to the analysts who are the primary customer of this work.

5.2 Future Model Developments

There are several developments planned for FY15. The first of these developments is to implement the model in an explicit code. Then we will perform further parameter fitting using the data made possible through the new diagnostics and additional creep testing. We will evaluate the regime over which the isotropic damage assumptions are valid. Finally, we will add experiments to the validation suite making the validation evidence for the model more robust and complete.

The model demonstrated in this report was implemented in an implicit code (Abaqus/Standard). We began with the implicit implementation because much of the analysis performed by W-13 is conducted with Abaqus/Standard. There are additional analyses performed in W-13 that require an explicit code. To satisfy the needs of W-13 we will implement this model in an explicit code (Abaqus/Explicit). We will then develop/support the hand off procedures required for performing initial analysis steps in Abaqus/Standard and then porting the results as initial conditions to Abaqus/Explicit.

Further parameter fitting will be possible because we are expecting simultaneous measurement of axial and radial strain under uniaxial cyclic loading. Hopefully, the additional diagnostics will provide us with volumetric strain data which will be used to inform the parameters in the flow potential as well as the shear/volumetric split of the viscoelastic and damage models.

The simulations performed in support of this document were all performed with fully integrated elements. Many analyses performed in W-13 will benefit from the ability to use reduced integration elements. To support that need we will study the appropriate hourglass control and advise the analysts as to the proper control and parameters.

Chapter 4 included simulations performed at different but constant temperatures. Testing of the model with components that are not appropriate for this report show reasonable convergence rates for conditions

with varying temperatures, but we intend to include derivatives of stress with respect to temperature in the implicit version of the model to improve the convergence rates for thermal-mechanical problems.

Bibliography

[1] *Numerical recipes in fortran 77: The art of scientific computing*, Cambridge University Press, 1992.

[2] Abaqus, *Abaqus theory manual*, Simulia, Providence, RI, version 6.10 ed., 2010.

[3] Raymond Canale AbaqusSteven Chapra, *Numerical methods for engineers*, 4th ed., McGraw Hill, 2002.

[4] F. L. Addessio and J. N. Johnson, *A constitutive model for the dynamic-response of brittle materials*, J. Appl. Phys. **67** (1990), no. 7, 3275–3286.

[5] J. G. Bennett, K. S. Haberman, J. N. Johnson, B. W. Asay, and B. F. Henson, *A constitutive model for the non-shock ignition and mechanical response of high explosives*, J. Mechanics Phys. Solids **46** (1998), no. 12, 2303–2322.

[6] M. Buechler, *Observed physical processes in mechanical tests of pbx9501 and recommendations for experiments to explore a possible plasticity/damage threshold*, Tech. Report LA-UR-12-21072, Los Alamos National Laboratory, 2012.

[7] M. A. Buechler, R. Deluca, and D. Thompson, *Review of cyclic experiments performed on pbx9501*, Tech. Report LA-UR-13-27212, Los Alamos National Laboratory, 2013.

[8] Miles A. Buechler and Darby J. Luscher, *A semi-implicit integration scheme for a combined viscoelastic-damage model of plastic bonded explosives*, Int. J. Numer. Meth Eng **99** (2014), no. 1, 54–78.

[9] Roylance David, *Engineering viscoelasticity*, 2001.

[10] T. Hughes J. Simo, *Computational inelasticity*, Springer, 1997.

[11] Rodrigue Desmorat Jean Lemaitre, *Engineering damage mechanics*, Springer, 2004.

[12] G. Johnson and W. Cook, *A constitutive model and data for metals subjected to large strains, high strain rates and high temperatures*, Quarterly Applied Mathematics **1** (1983), 541–547.

[13] Darby J. Luscher and Miles A. Buechler, *A semi-implicit integration scheme for stress update of viscoscram*, Tech. Report LA-UR-12-24915, Los Alamos National Laboratory, 2012.

[14] Ted Lyman, *Engineering validation test suite*, Lanl, Los Alamos, NM, revision 0.9 ed., 2014.

[15] D.C. Prager, *Soil mechanics and plastic analysis or limit design*, Quarterly Applied Mathematics **10** (1952), 157–165.

[16] R. Stevens, *Calibration of a viscoelastic model of pbx 9501*, Tech. Report LA-UR-13-20989, Los Alamos National Laboratory, 2013.